energies

MDPI

Article

Analysis of Power Coupling Characteristics and Decoupling Control Strategy for GFC Under Active Frequency and Voltage Support

Jun Yang [1], Siyi Chen [2], Jiatian Gan [1], Zhengkui Zhao [2], Yifei Wang [1] and Xiaoling Su [2,*]

[1] Electric Power Research Institute of State Grid Qinghai Electric Power Company, Xining 810008, China; 13109743069@163.com (J.Y.); dianaellena@126.com (J.G.); 13127150250@163.com (Y.W.)
[2] Key Laboratory of Smart Operation of New Energy Power System, Ministry of Education Qinghai University, Xining 810016, China; siyichen@mailbox.qhu.edu.cn (S.C.); zhaozhengkui@qhu.edu.cn (Z.Z.)
* Correspondence: suxiaoling@qhu.edu.cn

Abstract

Renewable energy is integrated into the grid through a grid-forming converter (GFC). The GFC can emulate synchronous generator (SG) characteristics. It can improve the stability and reliability of renewable power systems. However, the GFC has inherent coupling paths in its control structure. The mutual interaction between active and reactive power control loops is especially significant. It limits the power output of the GFC. It also limits the transient voltage support capability for the grid. Therefore, this paper first analyzes the effects of the active power control loop and the reactive power control loop on the power coupling characteristics of the GFC. A mathematical representation model is established. Second, this paper considers the active transient voltage support target of the GFC for the grid under large disturbance conditions. A power decoupling control strategy is proposed. It uses an improved power loop based on adaptive reactive power compensation (ARC). The equivalent active power difference and voltage deviation adaptively adjust the coefficient D_{qF}. This coefficient dynamically adjusts the reactive loop gain. Then transient voltage support and power decoupling are achieved. Finally, simulations and experiments verify the correctness of the proposed strategy.

Keywords: GFC; power coupling; frequency response; voltage support; adaptive reactive power compensation decoupling control

1. Introduction

With the increasing penetration of clean energy such as wind and photovoltaic power, the multi-stage energy conversion chain—from renewable generation and rectification/DC-link to inversion and grid connection—significantly affects the power coupling and active frequency/voltage support capability of grid-forming converters (GFCs). This conversion chain improves the security and stability of high-proportion renewable power systems [1–3]. On the other hand, while GFCs support grid voltage and frequency, they are also impacted by grid voltage and frequency variations [4,5]. In particular, under severe grid voltage sag faults, GFCs may experience sustained power oscillations and even instability [6].

GFCs can emulate the operating characteristics of a synchronous generator (SG). The grid-connected impedance is purely inductive. GFCs have good independent active and reactive power control capability [7]. However, they still face a problem in that the active power loop and reactive power loop cannot be controlled independently [8]. The GFC

Check for updates

Academic Editor: Kambiz Tehrani

Received: 21 September 2026
Revised: 21 October 2026
Accepted: 27 October 2026
Published: 29 October 2026

Copyright: © 2026 by the authors. Licensee MDPI, Basel, Switzerland. This article is an open access article distributed under the terms and conditions of the Creative Commons Attribution (CC BY) license.

regulates output active power. Its power angle changes. Its reactive power also changes. This affects the output capability of the whole generation unit [9,10]. On the other hand, the GFC supports grid voltage. The active–reactive power coupling phenomenon deteriorates the transient stability of the GFC. It affects the voltage support effect. It may even cause transient instability [11]. Therefore, finding an effective solution to the power coupling problem in the dynamic response of GFC grid-connected output is key to ensuring the stable operation of GFCs.

To analyze and solve the output power coupling problem of GFCs, reference [12] uses an active–reactive power variation matrix. It quantifies the power coupling strength. Then it proposes a virtual power control strategy. This strategy improves the power coupling problem under the GFC dynamic response. References [8,13] use a small-signal model. They prove that power coupling always exists. They adopt an adaptive virtual impedance method. This method performs offset control on the GFC output power angle. It improves the power decoupling effect. References [14,15] analyze voltage and current coordinate transformations. They introduce virtual power and virtual voltage to achieve power decoupling. However, the introduced virtual power and virtual voltage are fixed. They are greatly affected by the power angle variation range. Reference [16] designs a virtual impedance. It suppresses the power angle variation of the GFC under grid voltage sag faults. However, it also limits the reactive voltage support capability. The virtual impedance method is one of the current effective decoupling strategies [13,17]. Its control idea mainly makes the phase between the GFC internal voltage and the point of common coupling (PCC) voltage close to zero. This achieves better dynamic performance. However, under grid voltage sag faults, the internal voltage changes greatly. Therefore, the virtual impedance method is not suitable for power decoupling under GFC transient conditions [18].

For analysis of GFC transient stability and power coupling characteristics, reference [19] studies the influence of different control parameters on GFC transient stability through GFC dynamic response characteristics. Reference [20] proposes a flexible control strategy with adaptive switching of GFC internal voltage response speed. This method considers grid strength. It can maintain GFC system stability under different degrees of grid faults. It also provides active support required by the grid. References [21,22] propose a flexible switching control strategy for control parameters. This strategy is based on damping and inertia parameters in the active power loop. It improves power angle stability during GFC transient response. Then it improves GFC transient synchronization stability. References [23,24] use reactive current injection into the grid and correction of the voltage reference of the reactive power loop, respectively. These methods improve GFC stability under grid voltage sag faults. References [25–27] reveal the GFC transient process by methods such as the equal area criterion, energy function, and phase plane diagram. They further consider power coupling. They introduce the algebraic equation of a first-order reactive power loop. They construct a second-order differential equation for the GFC. This equation characterizes the active–reactive power coupling relationship. Reference [28] proves that power coupling further weakens GFC stability under grid voltage sag faults. It proposes a stability improvement method based on power dynamic compensation for grid voltage sag faults.

Based on the above research, this paper first considers the coupling relationship between the active and reactive power outputs of the GFC and establishes a power output model of the GFC, and then analyzes the degree of power coupling under different power angle magnitudes. Through the active power response model of the grid-connected GFC, the power angle variation trend under frequency response is analyzed. Furthermore, the transient response characteristics of the GFC under grid voltage sag faults are analyzed by using phase plane diagrams, and the active–reactive power steady-state curves and power angle curves under grid voltage sag faults are constructed, which reveals the influence

mechanism of the power angle on the power coupling and transient stability of the GFC. On this basis, combined with the active–reactive power coupling characteristics and the voltage vector relationship, the power loop is improved, and a power decoupling control strategy based on adaptive reactive power compensation (ARC) for the GFC, under active frequency and voltage support, is proposed to enhance the support capability and transient stability of the GFC.

2. Analysis of the GFC System and Coupling Characteristics

2.1. GFC Structure

The GFC grid-connected system is shown in Figure 1. The main circuit consists of a clean energy system, a DC capacitor, a three-level inverter circuit, an LC filter circuit, a transmission line, and an AC grid. The control circuit samples the three-phase voltage U_c and the three-phase current I_c at the PCC. These signals are used for power calculation. The instantaneous active power P_0 and the instantaneous reactive power Q_0 are obtained. The calculated instantaneous powers are processed by primary frequency regulation and primary voltage regulation. The modulation power angle δ and the modulation voltage E are obtained. Finally, the results are processed by virtual impedance control, voltage and current dual closed-loop control, and a PWM unit. The modulation signal is obtained. This modulation signal is fed back into the three-level inverter circuit.

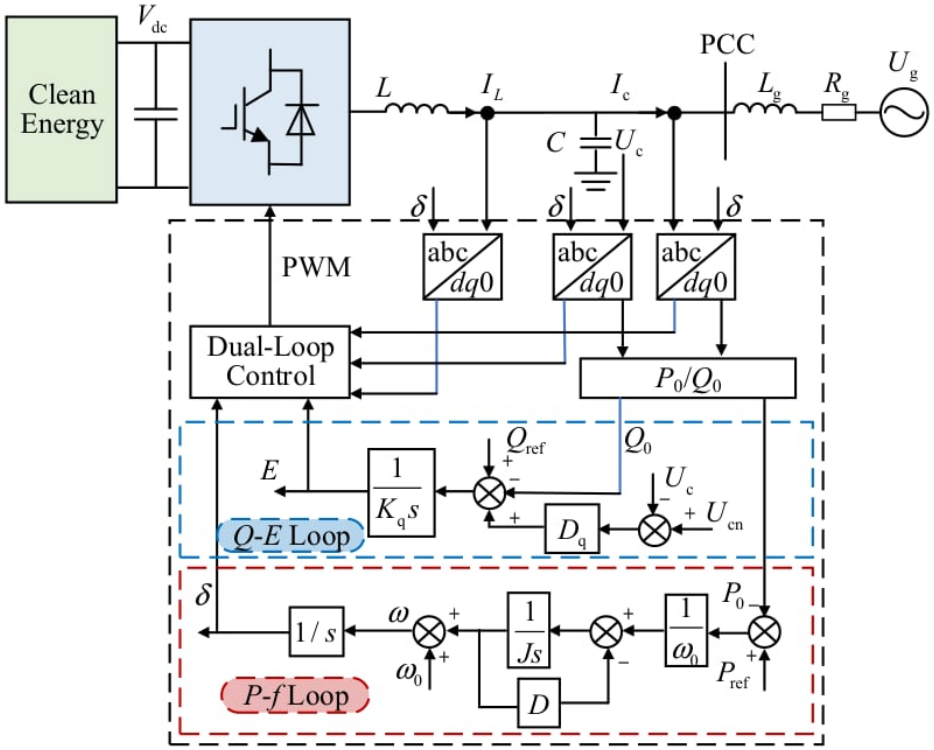


Figure 1. Main circuit topology of GFC.

As shown in Figure 1, the DC-side voltage V_{dc} is provided by clean energy. U_c is the GFC filter capacitor voltage. It is also the output voltage. U_g is the grid voltage at PCC. I_L and I_c are the filter inductor current and the GFC grid-connected current. L and C are the GFC filter inductance and capacitance. L_g and R_g are the line equivalent inductance and resistance. PWM is pulse width modulation.

The second-order differential equation of the GFC active power loop can be written as:

$$\begin{cases} J\frac{\mathrm{d}\Delta\omega}{\mathrm{d}t} = \frac{P_{\mathrm{ref}}}{\omega} - \frac{P_0}{\omega} - D(\omega - \omega_0) \\ \delta = \int \omega \mathrm{d}t \end{cases} \tag{1}$$

where J and D are the virtual inertia and virtual damping, respectively. ω, ω_0, and $\Delta\omega$ are the GFC output angular frequency, rated frequency, and their difference. P_{ref} is the active power reference. P_0 is the GFC output active power. δ is the converter output voltage phase. This is the reference phase.

The GFC reactive power loop usually adopts droop control. Its first-order differential equation is

$$E = \frac{1}{K_{\mathrm{q}}s}\left[Q_{\mathrm{ref}} - Q_0 + D_{\mathrm{q}}(U_{\mathrm{cn}} - U_{\mathrm{c}})\right] \tag{2}$$

where K_{q} is the integral coefficient. Q_{ref} and Q_0 are the reactive power reference and output reactive power, respectively. D_{q} is the reactive voltage regulation coefficient. U_{cn} is the voltage amplitude reference. E is the GFC internal voltage.

2.2. Analysis of GFC Power Coupling Characteristics

Figure 2 shows the equivalent circuit of the GFC grid-connected system. The GFC output voltage has amplitude U_{c} and phase δ. The line impedance can be expressed as $Z_{\mathrm{g}} = R_{\mathrm{g}} + jX_{\mathrm{g}}$; $X_{\mathrm{g}} = \omega L_{\mathrm{g}}$.

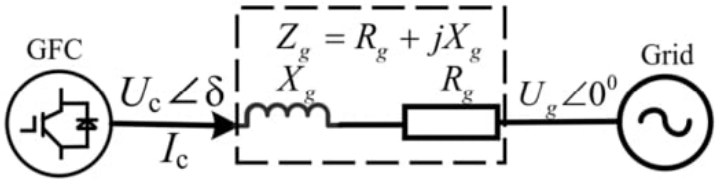


Figure 2. Equivalent circuit of GFC grid connection.

From Figure 2, the line current I_{c} can be expressed as:

$$I_{\mathrm{c}} = \frac{U_{\mathrm{c}}\angle\delta - U_{\mathrm{g}}\angle 0^{\circ}}{Z_{\mathrm{g}}\angle\theta} = \frac{U_{\mathrm{c}}}{Z_{\mathrm{g}}}\angle(\delta - \theta) - \frac{U_{\mathrm{g}}}{Z_{\mathrm{g}}}\angle(-\theta) \tag{3}$$

where Z_{g} and θ_{g} are the impedance magnitude and impedance angle.

From (3), the power fed by GFC into the grid is:

$$\begin{cases} P_0 = \frac{3U_{\mathrm{g}}}{2Z_{\mathrm{g}}}\left[U_{\mathrm{c}}\cos(\theta - \delta) - U_{\mathrm{g}}\cos\theta\right] \\ Q_0 = \frac{3U_{\mathrm{g}}}{2Z_{\mathrm{g}}}\left[U_{\mathrm{c}}\sin(\theta - \delta) - U_{\mathrm{g}}\sin\theta\right] \end{cases} \tag{4}$$

From (4), the partial derivatives of P_0 and Q_0 with respect to U_{c} and δ are:

$$\begin{cases} \frac{\partial P_0}{\partial \delta} = \frac{3U_{\mathrm{g}}U_{\mathrm{c}}}{2Z_{\mathrm{g}}}\sin(\theta - \delta) \\ \frac{\partial P_0}{\partial U_{\mathrm{c}}} = \frac{3U_{\mathrm{g}}}{2Z_{\mathrm{g}}}\cos(\theta - \delta) \\ \frac{\partial Q_0}{\partial \delta} = -\frac{3U_{\mathrm{g}}U_{\mathrm{c}}}{2Z_{\mathrm{g}}}\cos(\theta - \delta) \\ \frac{\partial Q_0}{\partial U_{\mathrm{c}}} = \frac{3U_{\mathrm{g}}}{2Z_{\mathrm{g}}}\sin(\theta - \delta) \end{cases} \tag{5}$$

From (5), U_{c} and δ are control variables. They act on P_0 and Q_0. The system has obvious coupling. It cannot achieve independent active and reactive power control.

Usually, $R_g \ll X_g$. Then Z_g can be approximated as X_g. At this time, $\theta_g \approx 90°$. Then the small-signal model of GFC output power can be obtained.

$$\begin{cases} \Delta P_0 = \frac{3U_g \sin\delta_0}{2X_g}\Delta U_c + \frac{3U_{cn}U_g \cos\delta_0}{2X_g}\Delta\delta \\ \Delta Q_0 = \frac{3U_g \cos\delta_0}{2X_g}\Delta U_c - \frac{3U_{cn}U_g \sin\delta_0}{2X_g}\Delta\delta \end{cases} \quad (6)$$

where δ_0 is the steady-state value of the GFC power angle. ΔU_c, $\Delta\delta$, ΔP_0, and ΔQ_0 are the small disturbance components of output voltage, power angle, active power, and reactive power, respectively.

From (6), active power is disturbed. ΔP_0 causes disturbances in ΔU_c and $\Delta\delta$. These disturbances affect ΔQ_0. Related studies show the following. Under small disturbance conditions, the influence of power angle on reactive power is greater than the influence of voltage on active power [8].

To further analyze the influence of $\Delta\delta$ and ΔU_c on power coupling, the relationships of ΔP_0 and ΔQ_0 with respect to ΔU_c and $\Delta\delta$ in (6) are plotted in Figure 3. The steady-state power angle operating point $\delta_0 = 0.035$ rad corresponds to planes P_1 and Q_1. The steady-state power angle operating point $\delta_0 = 0.175$ rad corresponds to planes P_2 and Q_2.

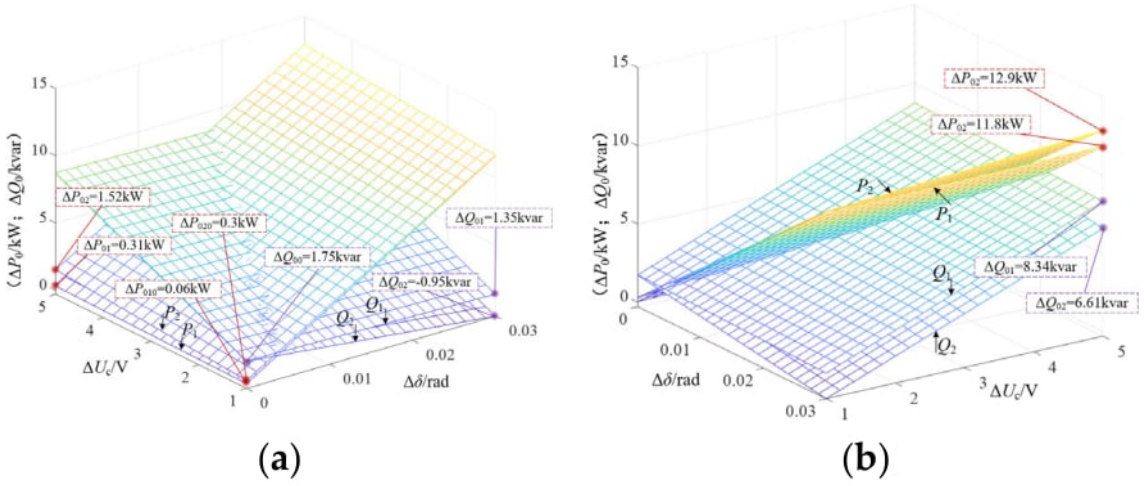


Figure 3. Influence of $\Delta\delta$ and ΔU_c on ΔP_0 and ΔQ_0. (**a**) 3D view (front perspective). (**b**) 3D view (side perspective).

From Figure 3, an increase in the steady-state power angle operating point significantly increases the reactive power deviation. From planes P_1 and P_1, active power is mainly affected by the variation of $\Delta\delta$. ΔU_c has little influence on active power output. From planes Q_1 and Q_2, the influence of $\Delta\delta$ variation on reactive power is more obvious. The $\Delta\delta$ caused by active power variation is the main factor of power coupling under GFC small disturbances.

2.3. Analysis of Coupling Characteristics Under GFC Frequency Response

Equations (1) and (4) are combined. $\theta \approx 90°$ is considered. Under small disturbances, the phase δ changes slightly. Thus, $\sin\delta \approx \delta$. The small-signal model expression of GFC output power P_0 can be obtained.

$$\begin{cases} P_0 = \frac{3U_cU_g}{2X_g}\sin\delta_i \approx K\delta \\ J\omega_0 s\Delta\omega = \Delta P_{ref} - \Delta P_0 - D\omega_0\Delta\omega \\ \Delta P_0 = K\Delta\delta = K\frac{\Delta\omega - \Delta\omega_{bus}}{s} \end{cases} \quad (7)$$

where ω_{bus} is the AC bus frequency.

From (7), the GFC active power closed-loop small-signal control block diagram is shown in Figure 4.

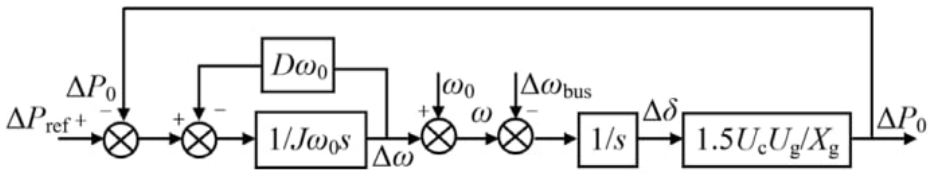


Figure 4. Small-signal control block diagram of GFC active power closed loop.

According to the active power control block diagram in Figure 4, the reference power–GFC frequency transfer function $G_p(s)$ can be obtained when P_{ref} changes. The grid-side frequency–GFC frequency transfer function $G_{\omega bus}(s)$ can be obtained when ω_{bus} is disturbed.

$$\begin{cases} G_p(s) = \frac{\Delta\omega}{\Delta P_{ref}}\Big|_{\omega_{bus}=0} = \frac{s}{J\omega_0 s^2 + D\omega_0 s + K} \\ G_{\omega_{bus}}(s) = \frac{\Delta\omega}{\Delta\omega_{bus}}\Big|_{\Delta P_{ref}=0} = \frac{K}{J\omega_0 s^2 + D\omega_0 s + K} \end{cases} \quad (8)$$

From (8), the step response curves of transfer functions $G_p(s)$ and $G_{\omega bus}(s)$ are shown in Figure 5.

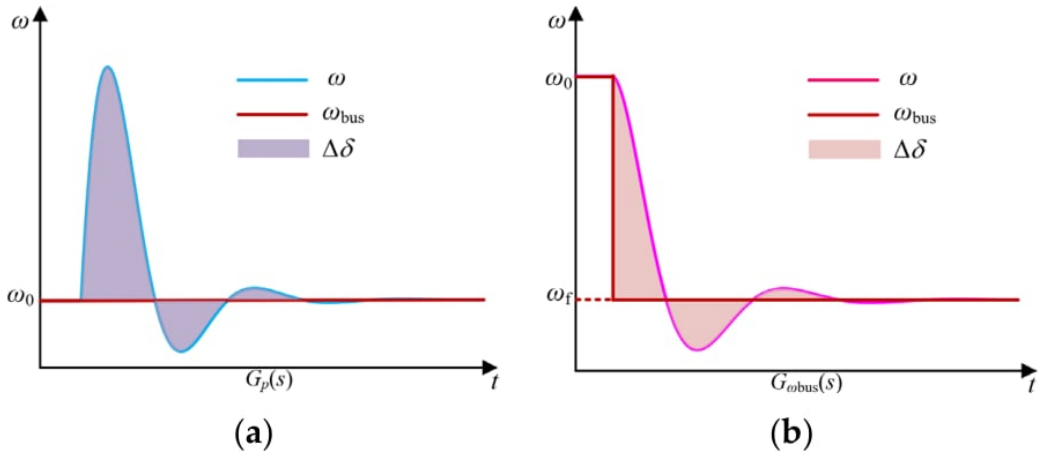


Figure 5. Step response curves of transfer functions $G_p(s)$ and $G_{\omega bus}(s)$. (**a**) Response curve of $G_p(s)$. (**b**) Response curve of $G_{\omega bus}(s)$.

For Figure 5a, which corresponds to $G_p(s)$, the active power reference is stepped up while the grid frequency is kept unchanged. The GFC output frequency first rises and then oscillates before settling, and the power angle deviation increases because it is the integral of the frequency deviation. Since the grid frequency is unchanged, the power angle variation is mainly determined by the GFC's own frequency response. For Figure 5b, which corresponds to $G_{\omega bus}(s)$, the grid frequency suddenly drops to a lower value. The GFC output frequency slowly tracks the new grid frequency. During this tracking process, a persistent frequency deviation exists between the GFC and the grid, and its integral produces an increasing power angle. Consequently, the GFC increases its active power output and provides frequency support.

The two subfigures together show that, whether the active power reference increases or the grid frequency changes, the frequency deviation is integrated into a power angle increase, and the increased power angle further causes reactive power deviation through the coupling path.

From Figure 5, the GFC output frequency curve ω is considered during the GFC dynamic response. According to the definition of $\Delta\delta$ in (7), the integral of the angular frequency deviation between ω and ω_{bus} is $\Delta\delta$. Figure 5a reflects the case after the active power command increases. At this time, $\Delta\omega_{bus} = 0$. Then $\Delta\delta$ is mainly determined by the GFC output frequency ω. When other control parameters remain unchanged, $\Delta\delta$ is positively correlated with the active power increase. Figure 5b reflects the case after the grid frequency suddenly drops to ω_f. The GFC output frequency ω slowly drops to ω_f. This reflects the frequency support capability of GFC. Therefore, a deviation still exists between ω and ω_{bus}. This deviation causes the power angle δ to increase. The active power fed by GFC into the grid increases. Active power frequency regulation is then achieved. It can be seen that in general, whether the active power reference increases or the grid-side frequency changes, the GFC output frequency changes. This increases the power angle. This increases the influence on power coupling.

3. Analysis of GFC Transient Stability and Power Coupling Characteristics

3.1. Analysis of GFC Transient Stability Characteristics

From (4), when $\theta \approx 90°$, the power fed by GFC into the grid is:

$$\begin{cases} P_0 = \frac{3U_c U_g \sin\delta}{2X_g} \\ Q_0 = \frac{3\left(U_c U_g \cos\delta - U_g^2\right)}{2X_g} \end{cases} \tag{9}$$

Based on (1), (2), and (9), the converter kinetic energy is zero. That is, $\omega - \omega_0 = 0$. Meanwhile, the GFC reactive power control loop stabilizes quickly under grid voltage sag faults. The derivative equation of GFC internal voltage E in (2) can be converted into a quasi-steady-state equation. E is treated as a parameter variable, not a state variable [29]. The following expression is obtained:

$$\begin{aligned} U_c = {} & \tfrac{1}{3}\left(1.5U_c\cos\delta - X_g D_q\right) \\ & + \tfrac{1}{3}\sqrt{\left(1.5U_c\cos\delta - X_g D_q\right)^2 + 6X_g\left(Q_{ref} + D_q U_{cn}\right)} \end{aligned} \tag{10}$$

Solve (1). The second-order differential equation of δ is obtained.

$$\ddot{\delta} = -\frac{D}{J}\dot{\delta} + \frac{1}{J\omega}(P_{ref} - P_0) \tag{11}$$

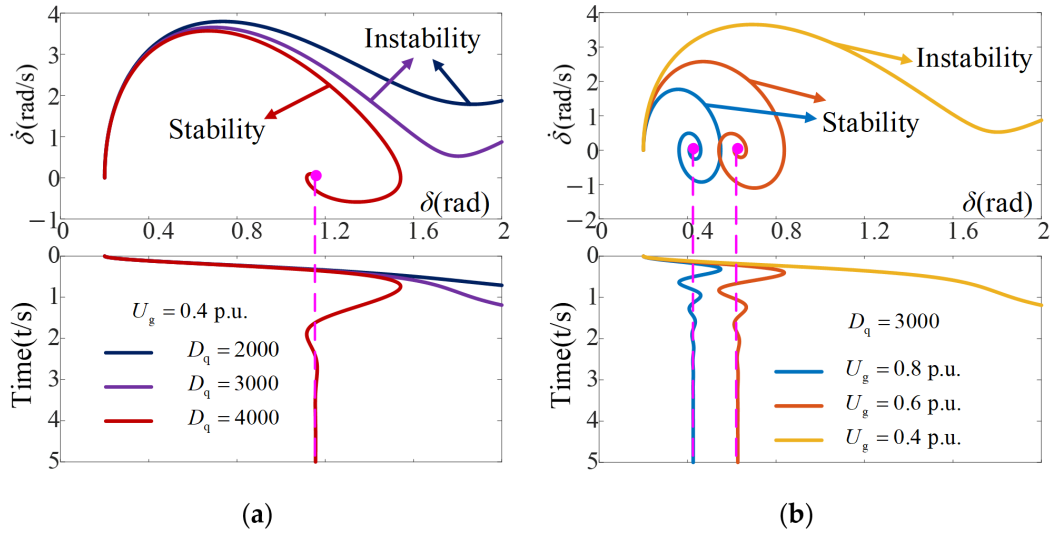
Substitute (2), (4), and (5) into (6). Then (12) is obtained.

$$\ddot{\delta} = -\frac{D}{J}\dot{\delta} + \frac{1}{J\omega_0}\left\{P_{ref} - \frac{U_g\sin\delta}{3X_g}\left[\begin{array}{l}\left(1.5U_c\cos\delta - X_g D_q\right) \\ +\sqrt{\begin{array}{l}\left(1.5U_c\cos\delta - X_g D_q\right)^2 \\ +6X_g(Q_{ref} + D_q U_{cn})\end{array}}\end{array}\right]\right\} \tag{12}$$

To obtain GFC transient characteristics under U_g sag faults, the GFC phase portrait power angle trajectory can be constructed by (12). The power angle trajectory in the phase portrait can determine whether GFC is transiently stable. Figure 6a shows the GFC power angle trajectories when U_g drops to 0.8 p.u., 0.6 p.u., and 0.4 p.u., respectively. When U_g = 0.8 p.u. and 0.6 p.u., the GFC power angle increases to a stable operating point. When U_g drops to 0.4 p.u., GFC is transiently unstable. The GFC power angle increases. No power angle stable operating point exists. GFC is transiently unstable.

From (12), D_q in the reactive power control loop is a key voltage support parameter of GFC. Its relationship with GFC stability under U_g sag is shown in Figure 6b. When U_g = 0.4 p.u. and D_q = 2000 and 3000, GFC is transiently unstable. When D_q = 4000, GFC has a transient power-angle-stable operating point. It can be seen that D_q is related to GFC

voltage support. It is also strongly related to GFC transient stability. Specifically, a larger D_q value can improve GFC transient stability.



(**a**) (**b**)

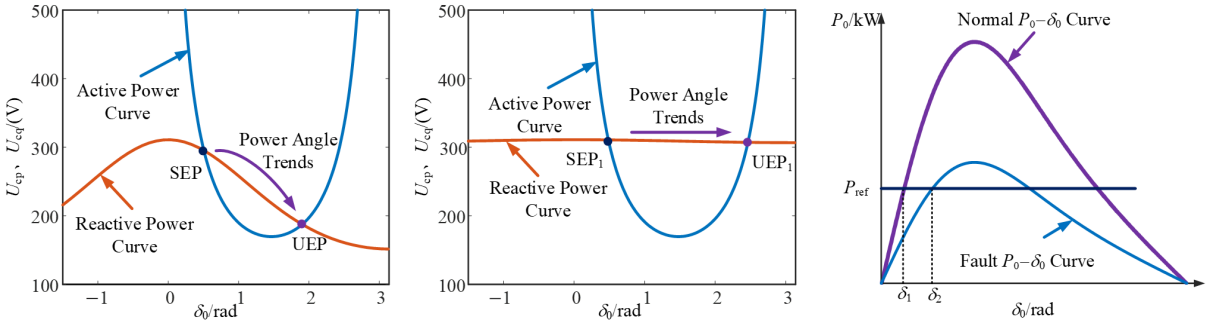
Figure 6. Power angle trajectory of GFC under grid voltage sag faults. (**a**) Different degrees of grid voltage sag faults. (**b**) Influence of D_q coefficient on GFC transient stability.

3.2. Analysis of GFC Transient Power Coupling Characteristics

From (9) and (10), the following expression is obtained:

$$\begin{cases} U_{cp} = \dfrac{P_{ref} X_g}{1.5 U_g \sin\delta} \\ U_{cq} = U_c \end{cases} \tag{13}$$

During grid voltage sag faults, the reactive voltage regulation coefficient can be increased. This increases the reactive power output. This helps support the grid voltage [11]. From (13), the power angle–voltage relationship under power coupling is obtained. It is shown in Figure 7a. Figure 7b shows the power angle–voltage relationship with increased D_q.



(**a**) (**b**) (**c**)

Figure 7. Analysis of influencing factors under power coupling. (**a**) Power steady-state curves. (**b**) Power steady-state curves with increased D_q. (**c**) P_0–δ_0 under grid voltage sag.

From Figure 7a, the steady-state curves of the active power loop and reactive power loop have two intersection points. They are the stable equilibrium point (SEP) and the unstable equilibrium point (UEP). From the power angle characteristic curve in Figure 7c, a grid voltage sag fault occurs. Then δ_1 increases to δ_2. This makes P_0 equal to P_{ref}. At this time, the PCC voltage decreases. The SEP moves toward the UEP. From Figure 7a,b, when

D_q is small, power coupling affects the system. The power angle difference between SEP and UEP is small. When D_q increases, the reactive power steady-state curve is approximately a straight line. At this time, GFC is approximately constant voltage control. The power angle difference between SEP and UEP increases significantly. The capability against U_g sag faults is significantly improved.

4. ARC-GFC Power Decoupling Control Design

From (4), during the GFC frequency response, increased active power causes reactive power deviation. This deviation is caused by power coupling in the reactive power dynamic response. To compensate for this deviation, the interaction between active power and reactive power is weakened. The reactive power value under power coupling is defined as Q_e. Then

$$Q_e = Q_0 + \Delta Q = Q_0 + \frac{\partial Q}{\partial \delta}\Delta\delta + \frac{\partial Q}{\partial U_c}\Delta U_c \tag{14}$$

If $Q_e = Q_0$, the following condition should be satisfied.

$$\Delta Q = \frac{\partial Q}{\partial \delta}\Delta\delta + \frac{\partial Q}{\partial U_c}\Delta U_c = 0 \tag{15}$$

Therefore, $\Delta\delta$ caused by active power variation is introduced into the reactive power control loop. This makes $\Delta Q = 0$. From (5) and (11), the improved equation with the reactive power loop is obtained.

$$\Delta U_c = \frac{U_c}{\tan(\theta - \delta)}\Delta\delta \tag{16}$$

From (16), when power variation causes $\Delta\delta$, ΔU_c should be introduced into the reactive power loop. According to the rule of (16), ΔU_c follows $\Delta\delta$. This makes $\Delta Q = 0$.

From Figure 7, power coupling still exists during GFC voltage support. The main reason is that δ increases under grid voltage sag faults. This makes GFC more easily transition from the transient SEP to the UEP. This causes GFC transient instability.

From Figure 1, the vector diagram of GFC under normal operation is obtained.

As shown in Figure 8, the coordinates of point B at the end of U_c are (x_U, y_U). According to the relationship between U_c and P_0 derived from Figure 2, the coordinate relationship is derived as follows.

$$\begin{cases} P_0 = \frac{3U_cU_g}{2X_g}\sin\delta = \frac{3U_g}{2X_g}y_U \\ y_U = \frac{P_0X_g}{1.5U_g} \end{cases} \tag{17}$$

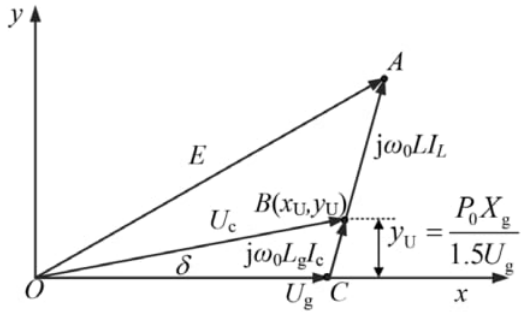


Figure 8. Vector diagram of GFC under normal operation.

When a grid voltage sag fault occurs, the vector diagram of GFC under fault operation is as follows.

From Figure 9, when grid voltage U_g drops to U_{gF}, U_c operates at point B_1. At this time, the power angle δ remains unchanged. U_c and U_g decrease. This causes output power P_0 to decrease at the fault instant. The reactive power control loop responds first. From (2), $K_q dE/dt > 0$. The internal voltage E increases rapidly to A'. Then the active power control loop begins to respond. The active power reference P_{ref} remains unchanged. If GFC finally stabilizes, the active power control continuously adjusts the power angle δ to δ'. This makes $P_0 = P_{ref}$. U_c finally stabilizes at U_{cF}. GFC transitions from the fault to a steady state. To reduce the power coupling degree under GFC transient faults and improve GFC stability, the D_q value can be adjusted. This makes the GFC internal voltage E increase rapidly. The active power difference decreases. Finally, a steady state is reached.

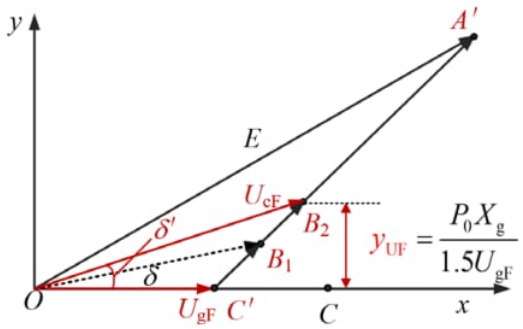


Figure 9. Vector diagram of GFC under grid voltage sag fault operation.

Based on the above, the GFC transient characteristics are summarized. A larger D_q reactive voltage control can obtain better voltage support. It can also achieve power decoupling in the GFC transient process. The maximum equivalent active power difference is used as the adaptive quantity. The ratio of the maximum active power variation to the difference between U_{cn} and U_c is defined as the D_q increment. To prevent the denominator from crossing zero, a deviation coefficient λ is set. The variable coefficient D_{qF} expression under ARC-GFC transient operation is constructed as follows.

$$\begin{cases} D_{qF} = D_q;\ U_c > 95\%U_{cn} \\ D_{qF} = D_q + \left|\frac{\max(P_{ref}-P_0)}{\lambda U_{cn}-U_c}\right|;\ U_c \le 95\%U_{cn} \end{cases} \quad (18)$$

From the above analysis, the ARC-GFC power decoupling control block diagram is shown in Figure 10. For more analysis of parameter perturbations for the strategy proposed in this paper, see Appendix A.

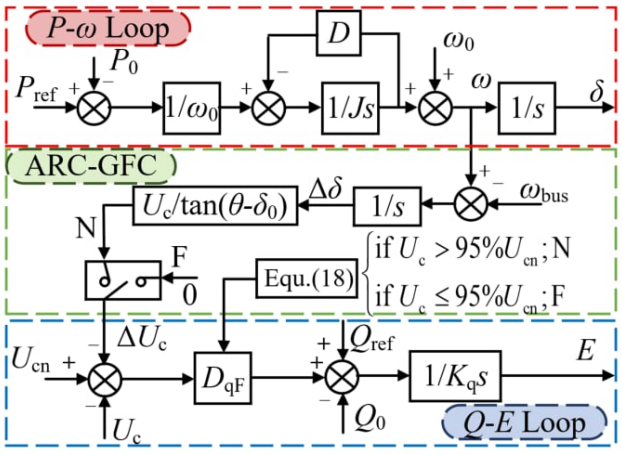


Figure 10. Block diagram of ARC-GFC power decoupling control strategy.

5. Simulation Verification

To verify the proposed ARC-GFC power decoupling control strategy under frequency and voltage support, a GFC grid-connected model is built using MATLAB/Simulink. The model is shown in Figure 1. The simulation parameters are listed in Table 1.

Table 1. Main control parameters of GFC.

Parameter	Value	Parameter	Value
V_{dc}	1.5 kV	U_g	311 V
E_0	380 V	ω_n	314 rad/s
Switching frequency	10 kHz	J	3 kg·m^2
L	0.4 mH	D	120 N·m·s/rad
L_g	1.2 mH	P_{ref}	200 kW
C	10 μF	D_q	3000
R_g	0.05 Ω	λ	1.01

5.1. Case 1: Active Power Reference Increase

Initially, the GFC output active power is 200 kW. At 1.5 s, the output active power increases by 50 kW. Figure 11a shows the GFC active power curve. The simulation results show that both control strategies can ensure that the GFC accurately tracks the active power output reference. In Figure 11, the GFC adopts the virtual synchronous generator (VSG) control strategy. The reactive power also increases when the active power increases. After the ARC-GFC decoupling control strategy is adopted, the GFC active power increases. Its reactive power quickly returns to the original operating point after the transient process. Figure 11c,d show the inverter output port voltage and current under the two control strategies. No obvious difference exists.

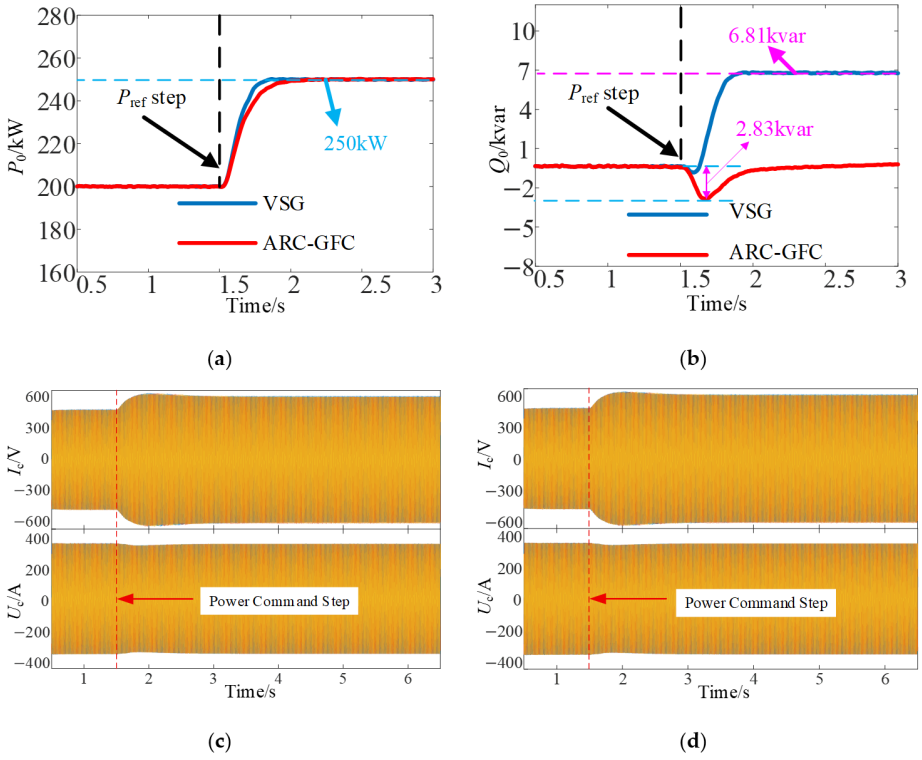


Figure 11. Power output effects under VSG control and ARC-GFC decoupling control when the given power increases. (**a**) GFC active power curve. (**b**) GFC reactive power curve. (**c**) GFC output waveforms under VSG control. (**d**) Output waveforms under ARC-GFC decoupling control.

5.2. Case 2: Grid Frequency Decrease

Figure 12 shows the GFC power curves under the grid frequency decrease condition. In Figure 12a, at 1.5 s, the grid frequency decreases by 0.15 Hz. Both control strategies achieve a GFC active power increase to 237 kW. These strategies are the VSG control strategy and the ARC-GFC decoupling control strategy. Figure 12b shows the following. GFC adopts the VSG control strategy. The grid frequency decreases. The output active power increases. At the same time, GFC reactive power also increases to 4.25 kvar. Voltage and current fluctuations intensify. They easily trigger overcurrent protection. They greatly weaken grid-forming support capability. In severe cases, they cause GFC disconnection. The inverter output port voltage and current under the two control strategies are shown in Figure 12c,d. Under ARC-GFC power decoupling control, GFC output reactive power returns to 0 after the transient process. This proves the effectiveness of the ARC-GFC decoupling control strategy.

5.3. Case 3: Grid Voltage Sag

Figure 13 shows the grid voltage drop. The grid voltage drops to 0.4 p.u. at t = 1.5 s. Figure 13 shows the following. GFC adopts VSG control. The system becomes unstable. GFC adopts the ARC-GFC decoupling control strategy. GFC always remains stable. Figure 13c,d show the following. The GFC voltage at the PCC amplitude increases significantly under decoupling control. The voltage support effect is obvious. The power angle stability margin is also better than that under the VSG control strategy. Figure 13e,f shows the GFC output voltage and current waveforms under the two control strategies, respectively. The simulation results show the following. Under the VSG control strategy, the GFC waveforms have an oscillation instability trend. Under ARC-GFC decoupling control, the GFC output voltage and current remain stable.

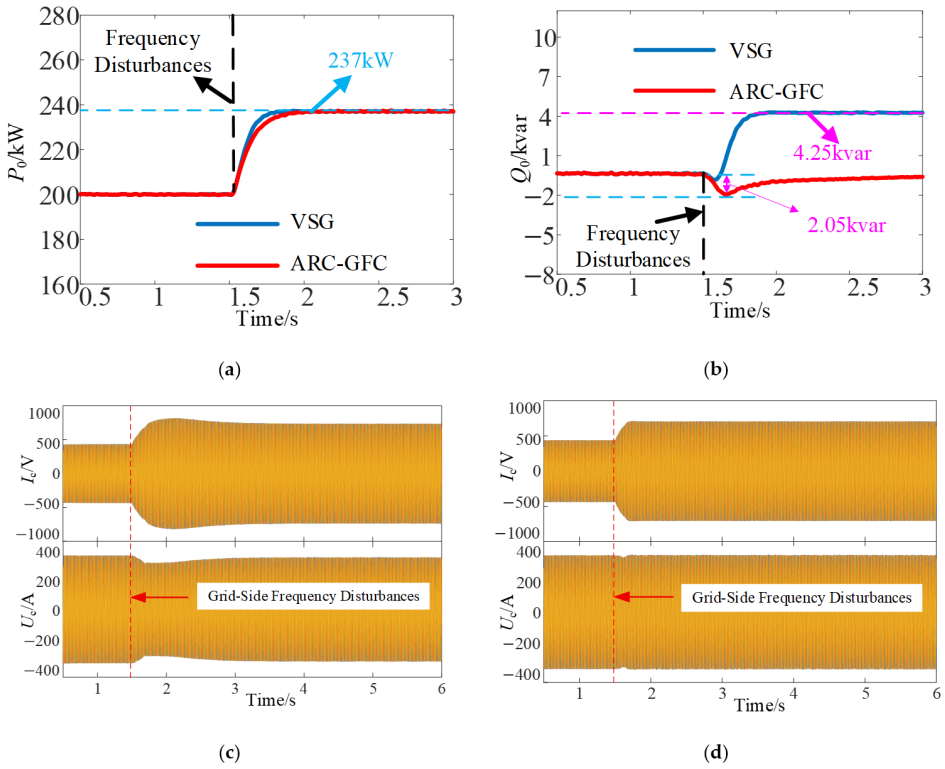


Figure 12. Power output effects under VSG control and ARC-GFC decoupling control when grid frequency decreases. (**a**) GFC active power curve. (**b**) GFC reactive power curve. (**c**) GFC output waveforms under VSG control. (**d**) Output waveforms under ARC-GFC decoupling control.

The total harmonic distortion (THD) is an important power-quality indicator for grid-connected converters [29]. The proposed ARC-GFC strategy does not change the main circuit topology, the PWM modulation scheme, or the output filter parameters; therefore, the steady-state switching harmonic characteristics of the GFC are essentially the same as those of the conventional VSG. The adaptive law mainly adjusts the reactive power loop gain during disturbances, and its saturation limits prevent excessive variations of the internal voltage and current. FFT analysis of the PCC voltage and GFC output current under steady-state and grid voltage sag conditions shows that the THD increases only briefly during transients and returns to the steady-state level afterward, with no sustained low-order harmonic component observed. Hence, the proposed ARC-GFC achieves effective power decoupling and transient voltage support without significantly deteriorating the harmonic performance of the GFC.

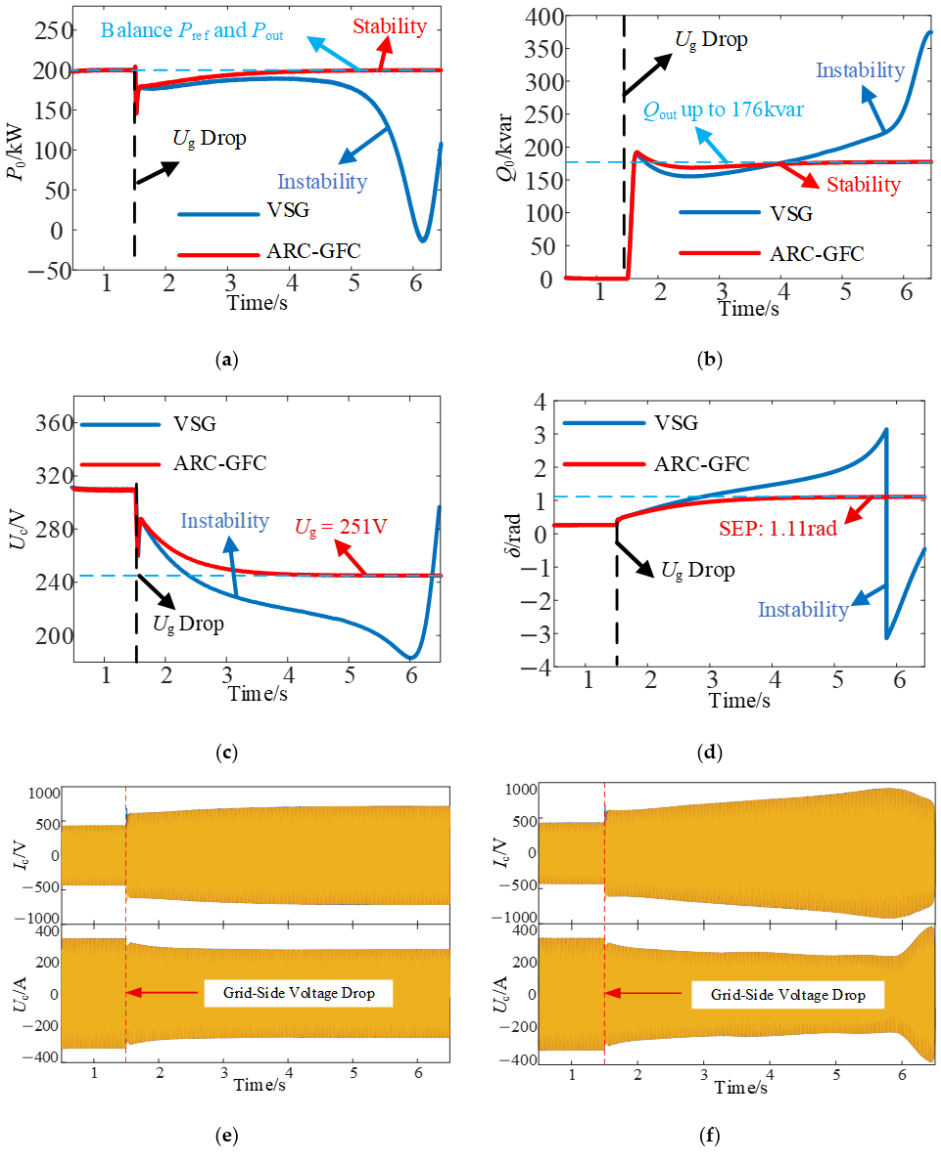


Figure 13. Waveform output effects under VSG control and ARC-GFC decoupling control when the grid voltage sags. (**a**) GFC active power curve. (**b**) GFC reactive power curve. (**c**) GFC voltage amplitude curve. (**d**) GFC power angle curve. (**e**) GFC output waveforms under VSG control. (**f**) Output waveforms under ARC-GFC decoupling control.

6. Experimental Verification

This paper builds an experimental verification model based on the StarSim hardware-in-the-loop (HIL) semi-physical simulation platform. The model is shown in Figure 14. The host computer is a PC. The slave computer consists of an HIL real-time simulator and an RCP programmable controller. The host computer and the slave computer are connected through a signal switch. The main circuit runs on the HIL real-time simulator. The control circuit runs on the RCP programmable controller. The main circuit and the control circuit are connected through an I/O junction box. For the experimental parameters, refer to Table 1.

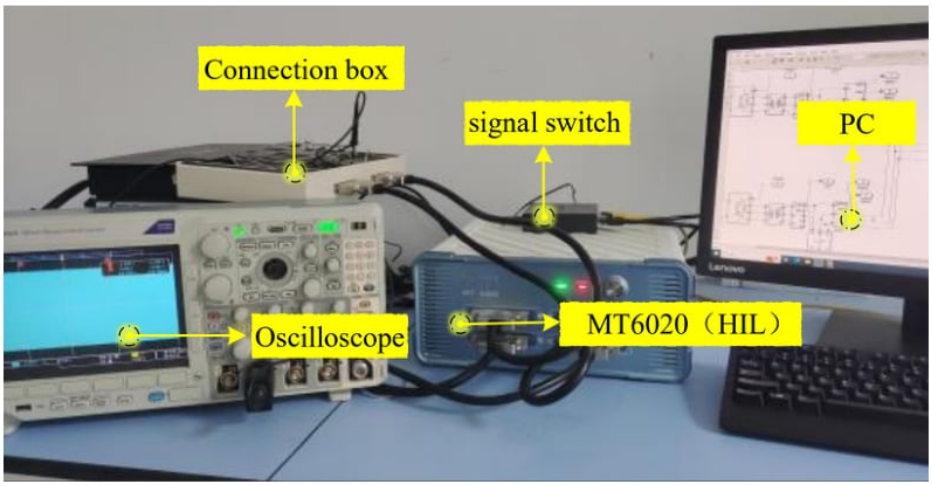


Figure 14. Waveform output effects under VSG control and ARC-GFC decoupling control when grid voltage sags.

Figures 15 and 16 show the experimental waveforms under Case 1 and Case 2, respectively. From Figures 15a and 16a, both active power increase and frequency cause the GFC power angle to increase. This causes reactive power variation. The active–reactive power coupling is obvious. From Figures 15b and 16b, when ARC-GFC power decoupling control is introduced, the GFC power angle increment $\Delta\delta$ remains unchanged under Case 1 and Case 2. In Case 1, the active power increases to 1.25 p.u. In Case 2, the active power increases to 1.18 p.u. The reactive power returns to the initial value after a short transient process. After ARC-GFC power decoupling control is introduced, active and reactive power achieve power decoupling under Case 1 and Case 2.

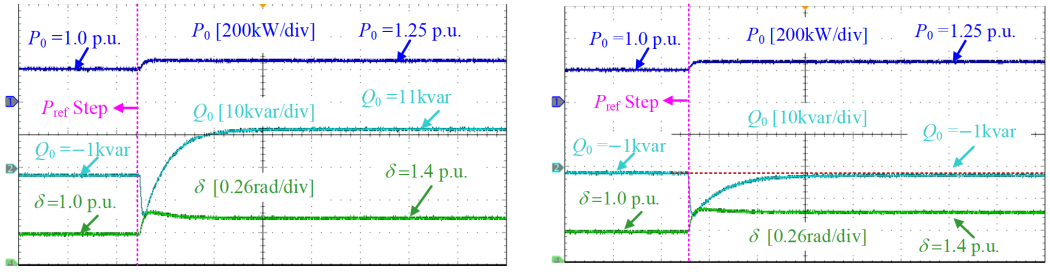


Figure 15. GFC output waveforms under Case 1. (**a**) GFC output waveforms under VSG control. (**b**) Output waveforms under ARC-GFC decoupling control.

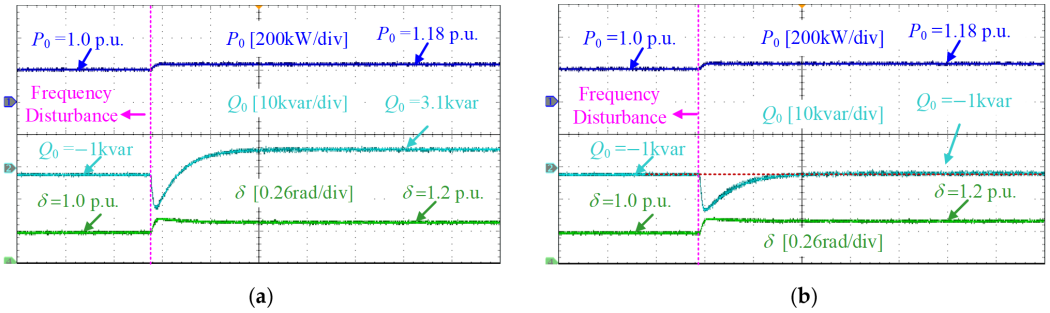


Figure 16. GFC output waveforms under Case 2. (**a**) GFC output waveforms under VSG control. (**b**) Output waveforms under ARC-GFC decoupling control.

Figure 17 shows the GFC experimental output waveforms under Case 3 when the grid-side voltage drops to 0.4 p.u. From Figure 17a, under VSG control, the GFC output voltage continuously decreases. This finally causes an imbalance between the active power reference and the output. Voltage and power oscillations occur. The GFC system is transiently unstable. From Figure 17b, after ARC-GFC power decoupling control is introduced, the system output voltage still decreases. However, it finally stabilizes at 0.82 p.u. The active power returns to the initial value after the dynamic response of the grid-side voltage sag. The reactive power increases to 19.8 kvar. The reactive voltage support capability is significantly improved. The GFC system is transiently stable.

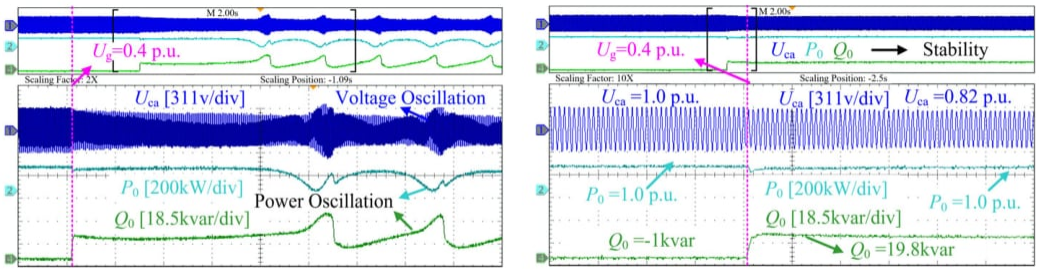


Figure 17. GFC output waveforms under Case 3. (**a**) GFC output waveforms under VSG control. (**b**) Output waveforms under ARC-GFC decoupling control.

7. Conclusions

This paper addresses the influence of power coupling on the frequency and voltage support capability of GFCs. It analyzes the influence mechanism of power coupling on GFC frequency response and voltage support. It proposes a decoupling control strategy that considers frequency and voltage support characteristics. The main conclusions are as follows:

(1) Power coupling of the GFC always exists. When the power angle is too large, the coupling phenomenon is more severe. Active power increase and frequency response of the GFC both increase the power angle. This aggravates power coupling. It affects the dynamic performance of the GFC.

(2) Under grid voltage sag faults, the reactive voltage regulation coefficient can improve the transient stability and voltage support capability of the GFC. During voltage support of the GFC, the coupling of active and reactive power deteriorates its transient stability. Increasing the reactive voltage regulation coefficient can also weaken its power coupling characteristics.

(3) Based on the reactive and active power control equations, this paper proposes the ARC-GFC decoupling control strategy. This strategy can weaken the influence of power

coupling of the GFC under frequency and voltage support conditions. It improves the response characteristics and stability of the GFC.

Author Contributions: J.Y. and S.C. developed the conceptualization and formulated the overall research framework. J.Y. was primarily responsible for the mathematical modeling, optimization formulation, software implementation, and project administration, while S.C. contributed to model development, analytical refinement, and validation of the proposed methodology. J.G. was responsible for data curation and investigation. Z.Z. supported data curation and validation of the results. Y.W. contributed to formal analysis and visualization of the simulation results. J.Y. and S.C. prepared the original manuscript. J.Y., S.C., J.G., Z.Z., Y.W. and X.S. contributed to manuscript review and editing. X.S. provided supervision, funding acquisition, and project administration. All authors have read and agreed to the published version of the manuscript.

Funding: This work was supported by the Science and Technology Project of State Grid Qinghai Electric Power Company (Key Technologies for Grid-Connection Control and Testing of Active-Support Photovoltaic Inverters in Weak Grid Environments, Grant No. 522807260001).

Data Availability Statement: The original contributions presented in this study are included in the article. Further inquiries can be directed to the corresponding authors.

Acknowledgments: The authors would like to express their sincere gratitude to the participating institutions for the valuable support and assistance provided throughout this research.

Conflicts of Interest: Authors Jun Yang, Jiatian Gan, and Yifei Wang were employed by the Electric Power Research Institute of State Grid Qinghai Electric Power Company. The remaining authors declare that the research was conducted in the absence of any commercial or financial relationships that could be construed as potential conflicts of interest. The authors declare that this study received funding from State Grid Qinghai Electric Power Company. The funder was not involved in the study design, data collection, analysis, interpretation of data, the writing of this article, or the decision to submit it for publication, except for the aforementioned individual contributions of the employed authors.

Appendix A

Analysis of Parameter Perturbations for the Strategy Proposed in This Paper

Appendix A.1. Stability Verification Based on Equations (8) and (18)

The parameters J, D, and K were varied separately, and six Bode plots were obtained: three for $G_{\mathrm{p}}(s)$ and three for $G_{\omega\mathrm{bus}}(s)$. Since the adaptive coefficient D_{qF} changes the internal voltage U_{c} and thus changes K, the variation of K covers the parameter range introduced by the adaptive law.

The six Bode plots consistently show that, over the entire adaptive range, both transfer functions maintain positive gain margins and positive phase margins. The closed-loop poles remain in the left half-plane, and the resonant peaks are bounded. No right-half-plane poles or phase-crossover-induced instability were observed. This indicates that the adaptive variation of D_{qF} does not destabilize the closed-loop system from the small-signal perspective. The saturation limits of the adaptive law further guarantee that K remains within a bounded range, so the frequency domain stability conclusion holds for the complete adaptation range.

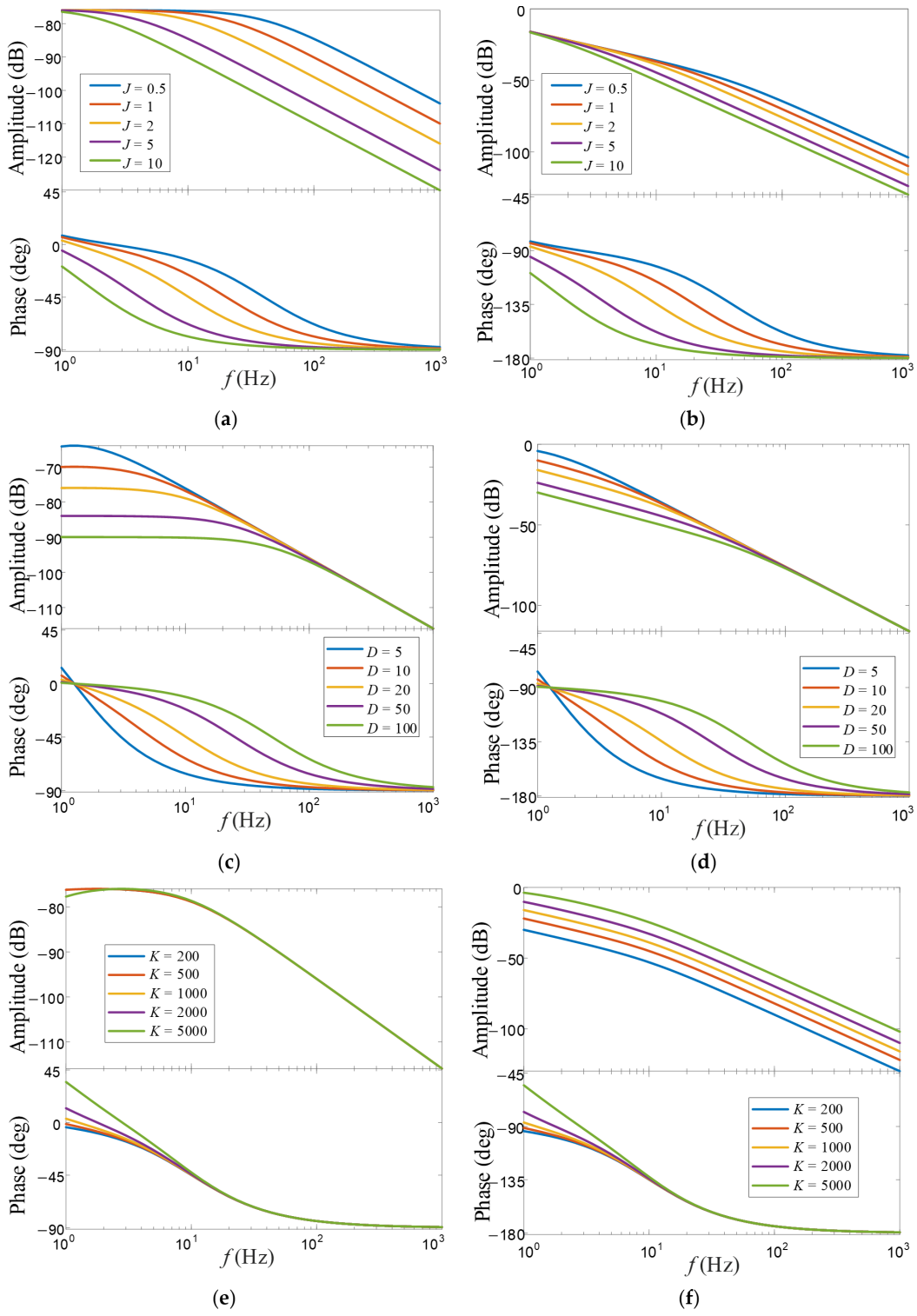


Figure A1. Frequency domain stability verification based on Equation (8). (**a**) Bode Plot of $G_p(s)$ as a Function of J. (**b**) Bode Plot of $G_{\omega bus}(s)$ as a Function of J. (**c**) Bode Plot of $G_p(s)$ as a Function of D. (**d**) Bode Plot of $G_{\omega bus}(s)$ as a Function of D. (**e**) Bode Plot of $G_p(s)$ as a Function of K. (**f**) Bode Plot of $G_{\omega bus}(s)$ as a Function of K.

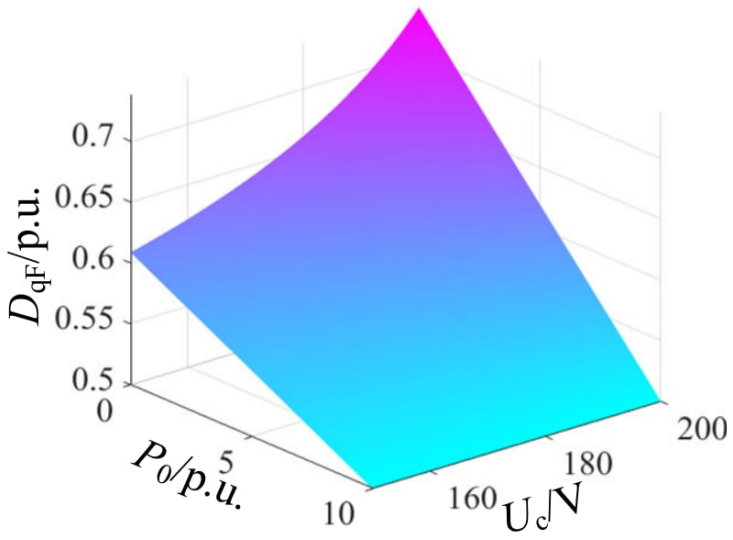


Figure A2. Three-dimensional parametric stability boundary analysis based on Equation (18).

Figure A2 shows that, under the action of the adaptive Equation (18), the trajectory of D_{qF} always remains inside the stable region. When a disturbance causes P_0 or Uc to deviate, the adaptive law increases D_{qF}, which moves the system trajectory further into the interior of the stable region rather than across the stability boundary. Therefore, the closed-loop system remains stable throughout the implementation of the adaptive law. This provides direct evidence that the adaptive variation of the reactive power control coefficient does not destabilize the system.

Appendix A.2. Simulation Analysis Under Different Parameters

We have reduced the gains of the current loop and voltage loop and repeated the simulations of Figure 11 (P_{ref} step) and Figure 12 (frequency disturbance). The results are summarized as follows:

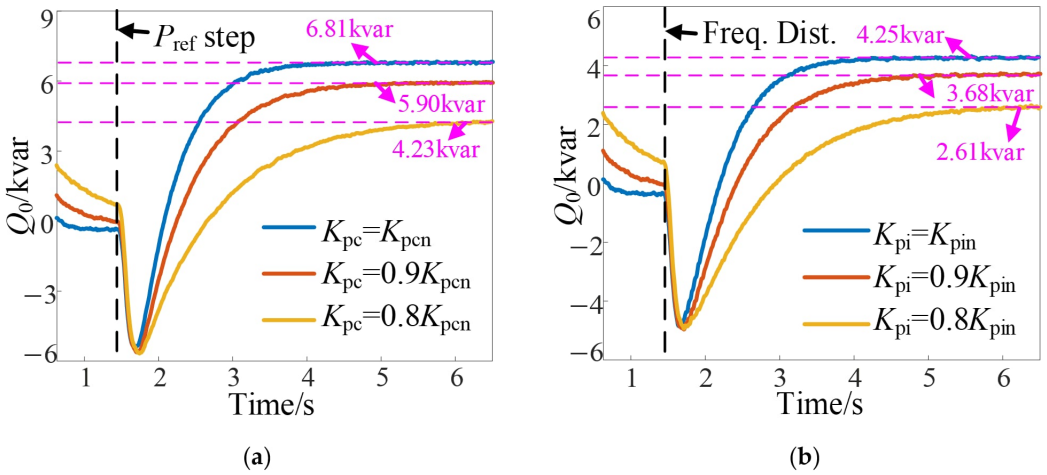


Figure A3. Q_0 output with reduced voltage and current loop gains. (**a**) Q_0 output with reduced voltage loop gain. (**b**) Q_0 output with reduced current loop gain.

After reducing the inner-loop gains, the reactive power deviation still exists. The settling time becomes longer, but the steady-state reactive power error remains, which confirms that the coupling is not caused by the inner-loop gains.

These results clearly demonstrate that the effectiveness of the proposed ARC-GFC is not a consequence of high-gain inner-loop controllers. The decoupling is achieved by

the adaptive reactive power compensation law, which is independent of the inner-loop bandwidth.

When the grid inductance L_g increases in a weak grid, the line reactance X_g increases, which leads to a larger steady-state power angle δ for the same power transfer. As analyzed in Section 2.2 and Figure 3 of the manuscript, a larger power angle aggravates the coupling between active and reactive power. In addition, the grid inductance can form an LC resonance with the filter capacitor C, potentially causing harmonic amplification or oscillation if the resonance frequency falls within the control bandwidth. The proposed ARC strategy adjusts the reactive loop gain D_{qF} adaptively based on the active power difference and voltage deviation. Since the ARC loop operates on the fundamental power angle relationship, its adaptive nature provides a certain degree of robustness against grid inductance variation.

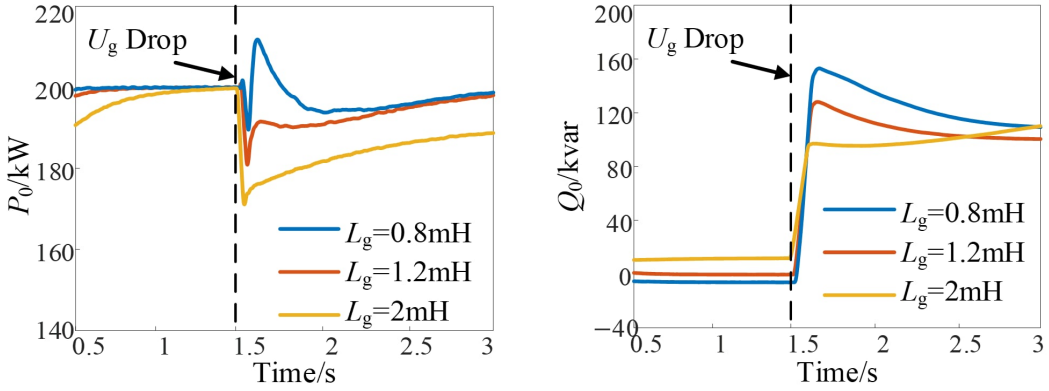


Figure A4. P_0 and Q_0 output with reduced L_g. (**a**) Active power output with reduced L_g. (**b**) Reactive power output with reduced L_g.

Load switching at the PCC causes voltage fluctuations and power demand changes, which affect the GFC output power and power angle. The ARC strategy dynamically increases the reactive power support during voltage sags, which can help maintain PCC voltage and reduce power coupling. However, sudden load changes may still cause transient coupling and require proper tuning of the adaptive coefficient.

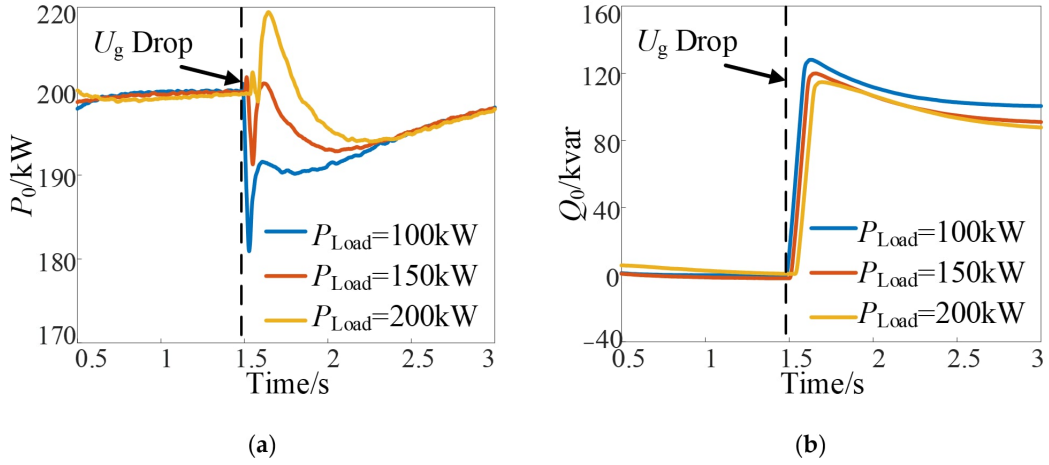


Figure A5. P_0 and Q_0 output with reduced P_{Load}. (**a**) Active power output with reduced P_{Load}. (**b**) Reactive power output with reduced P_{Load}.

References

1. Rathnayake, D.B.; Razzaghi, R.; Bahrani, B. Generalized virtual synchronous generator control design for renewable power systems. *IEEE Trans. Sustain. Energy* **2022**, *13*, 1021–1036. [CrossRef]
2. Tehrani, K.A.; Rasoanarivo, I.; Andriatsihoarana, H.; Sargos, F.M. A new multilevel inverter model NP without clamping diodes. In Proceedings of the 2008 34th Annual Conference of IEEE Industrial Electronics, Orlando, FL, USA, 10–13 November 2008; pp. 466–472.
3. Wu, H.; Liu, J.; Zeng, Z. Improved virtual synchronous generator control for grid-forming converters in weak grids. *IEEE Trans. Energy Convers.* **2021**, *36*, 2063–2074.
4. Qiu, M.H.; Han, Y.D.; Zhao, Y.X. Concepts, key issues, and development pathways for building a new power system. *CSEE* **2022**, *42*, 6677–6690.
5. Wang, M.; Chen, A.; Huang, Y.; Pang, X.; Cheng, C.; Liu, T. Wide-Frequency Power Decoupling and Accurate Reactive Power Control for Andronov–Hopf Virtual Oscillator-Based Grid-Forming Inverters. *IEEE Trans. Power Electron.* **2026**, *4*, 5932–5945. [CrossRef]
6. Chen, S.; Gan, J.; Zhao, Z.; Su, X.; Chen, L.; Geng, Z. Phase lead compensation based control strategy for D-PMSG DC-link dynamic response improvement. *Electr. Power Syst. Res.* **2026**, *260*, 113363. [CrossRef]
7. Fan, C.; Qin, X.; Qi, L. Role improvements and research prospects of virtual impedance in grid-forming droop control. *Power Sys. Technol.* **2024**, *48*, 2237–2250.
8. Huang, M.; Shu, S.R.; Li, X.L. A review of synchronization-stability-oriented analysis and control of power electronic grid-connected converters. *Trans. China Electrotech. Soc.* **2024**, *39*, 5978–5994.
9. Li, M.X.; Wang, Y.; Hu, W.H. Unified modeling and analysis of dynamic power coupling for grid-forming converters. *IEEE Trans. Power Electron.* **2022**, *37*, 2321–2337. [CrossRef]
10. Tian, Y.; Xu, X.; Wang, Y.; Li, Z.; Zhang, Z.; Gao, Y. Full-State Feedback Power Decoupling Control for Grid Forming Converter With Improved Stability and Inertia Response. *IEEE Trans. Power Electron.* **2025**, *2*, 2930–2942. [CrossRef]
11. Long, B.; Zhu, S.; Rodriguez, J.; Guerrero, J.M.; Chong, K.T. Enhancement of power decoupling for virtual synchronous generator: A virtual inductor and virtual capacitor approach. *IEEE Trans. Ind. Electron.* **2023**, *70*, 6830–6843. [CrossRef]
12. Yang, Y.Q.; Xu, J.Z.; Li, C. A new virtual inductance control method for frequency stabilization of grid-forming virtual synchronous generators. *IEEE Trans. Ind. Electron.* **2023**, *70*, 441–451. [CrossRef]
13. Mahmoud, A.E.; Amr Ahmed, A.R.; Yasser Abdel-Rady, I.M. Analysis and weakening of sequence impedance coupling in grid-forming converters. *IEEE Trans. Power Deliv.* **2024**, *39*, 3292–3304. [CrossRef]
14. Dong, N.B.; Li, M.F.; Chang, X.F. Robust power decoupling based on feedforward decoupling and extended state observers for virtual synchronous generator in weak grid. *IEEE J. Emerg. Sel. Top. Power Electron.* **2023**, *11*, 576–587. [CrossRef]
15. Zhang, Z.; Fang, J.; Zhang, C.; Fu, C.; Blaabjerg, F. A Robust Singular Perturbation Method for Decoupling of Power and Voltage Control of Grid-Forming Converters. *IEEE Trans. Smart Grid* **2026**, *2*, 1291–1302. [CrossRef]
16. Meng, Z.; Xing, X.; Ren, Q. A Decoupling Control Method for Virtual Synchronous Generator With Voltage Feedforward Compensation and Virtual Inductor. *IEEE Trans. Power Electron.* **2026**, *4*, 6179–6195. [CrossRef]
17. Wang, Z.; Wang, Y.; Davari, M.; Blaabjerg, F. An effective PQ -decoupling control scheme using adaptive dynamic programming approach to reducing oscillations of virtual synchronous generators for grid connection with different impedance types. *IEEE Trans. Ind. Electron.* **2024**, *71*, 3763–3775. [CrossRef]
18. Chen, M.; Zhou, D.; Tayyebi, A.; Prieto-Araujo, E.; Dorfler, F.; Blaabjerg, F. Generalized multivariable grid-forming control design for power converters. *IEEE Trans. Smart Grid* **2022**, *13*, 2873–2885. [CrossRef]
19. Wu, H.; Wang, X. Design-Oriented Transient Stability Analysis of Grid-Connected Converters with Power Synchronization Control. *IEEE Trans. Ind. Electron.* **2018**, *66*, 6473–6482. [CrossRef]
20. Wu, H.; Wang, X. Control of Grid-Forming VSCs: A Perspective of Adaptive Fast/Slow Internal Voltage Source. *IEEE Trans. Power Electron.* **2023**, *38*, 10151–10169. [CrossRef]
21. Mohammed, N.; Ciobotaru, M. Adaptive power control strategy for smart droop-based grid-connected inverters. *IEEE Trans. Smart Grid* **2022**, *13*, 2075–2085. [CrossRef]
22. Alipoor, J.; Miura, Y.; Ise, T. Power System Stabilization Using Virtual Synchronous Generator With Alternating Moment of Inertia. *IEEE J. Emerg. Sel. Top. Power Electron.* **2015**, *3*, 451–458. [CrossRef]
23. Koiwa, K.; Inoo, K.; Zanma, T.; Liu, K.Z. Virtual voltage control of VSG for overcurrent suppression under symmetrical and asymmetrical voltage dips. *IEEE Trans. Ind. Electron.* **2021**, *69*, 11177–11186. [CrossRef]
24. Wang, P.; Chen, M.; Wang, J.; Zhu, G.; Jiang, F. An active power feedforward compensation-based power decoupling method for droop control converters. *IEEE Trans. Power Electron.* **2025**, *40*, 6726–6739. [CrossRef]
25. Wang, X.; Taul, M.G.; Wu, H.; Liao, Y.; Blaabjerg, F.; Harnefors, L. Grid-synchronization stability of converter-based resources: An overview. *IEEE Open J. Ind. Appl.* **2020**, *1*, 115–134. [CrossRef]

26. Yang, J.; Chi, K.T.; Huang, M.; Fu, X. Homoclinic bifurcation of a grid-forming voltage source converter. *IEEE Trans. Power Electron.* **2021**, *36*, 13176–13187. [CrossRef]
27. Lou, G.; Yang, Q.; Gu, W.; Zhang, J. An improved control strategy of virtual synchronous generator under symmetrical grid voltage sag. *Int. J. Electr. Power Energy Syst.* **2020**, *121*, 106093. [CrossRef]
28. Zhu, D.; Li, X.; Zhou, S.; Zhong, X.; Zou, X.; Kang, Y. Optimized Power Decoupling Control for Grid-Forming Converter Under Different R/X Ratios of Grid Impedance. *IEEE Trans. Circuits Syst. II Express Briefs* **2025**, *12*, 2052–2056. [CrossRef]
29. Alawieh, H.; Tehrani, K.A.; Azzouz, Y.; Dakyo, B. A new active common-mode voltage elimination method for three-Level Neutral-Point Clamped inverters. In Proceedings of the IECON 2014—40th Annual Conference of the IEEE Industrial Electronics Society, Dallas, TX, USA, 29 October–1 November 2014; pp. 1060–1066.

Disclaimer/Publisher's Note: The statements, opinions and data contained in all publications are solely those of the individual author(s) and contributor(s) and not of MDPI and/or the editor(s). MDPI and/or the editor(s) disclaim responsibility for any injury to people or property resulting from any ideas, methods, instructions or products referred to in the content.